

# Reduction of frame rate in full-field swept-source optical coherence tomography by numerical motion correction [Invited]

CLARA PFÄFFLE,<sup>1,\*</sup> HENDRIK SPAHR,<sup>2</sup> DIERCK HILLMANN,<sup>3</sup>  
HELGE SUDKAMP,<sup>1</sup> GESA FRANKE,<sup>1,2</sup> PETER KOCH,<sup>1</sup> AND  
GEREON HÜTTMANN<sup>1,2,4</sup>

<sup>1</sup>Medical Laser Center Lübeck GmbH, Peter-Monnik-Weg 4, Lübeck, Germany

<sup>2</sup>University of Lübeck, Institute of Biomedical Optics, Peter-Monnik-Weg 4, Lübeck, Germany

<sup>3</sup>Thorlabs GmbH, Maria-Goeppert-Straße 9, Lübeck, Germany

<sup>4</sup>Airway Research Center North (ARCN), Member of the German Center for Lung Research (DZL), Germany

\*clara.pfaeffle@student.uni-luebeck.de

**Abstract:** Full-field swept-source optical coherence tomography (FF-SS-OCT) was recently shown to allow new and exciting applications for imaging the human eye that were previously not possible using current scanning OCT systems. However, especially when using cameras that do not acquire data with hundreds of kHz frame rate, uncorrected phase errors due to axial motion of the eye lead to a drastic loss in image quality of the reconstructed volumes. Here we first give a short overview of recent advances in techniques and applications of parallelized OCT and finally present an iterative and statistical algorithm that estimates and corrects motion-induced phase errors in the FF-SS-OCT data. The presented algorithm is in many aspects adopted from the phase gradient autofocus (PGA) method, which is frequently used in synthetic aperture radar (SAR). Following this approach, the available phase errors can be estimated based on the image information that remains in the data, and no parametrization with few degrees of freedom is required. Consequently, the algorithm is capable of compensating even strong motion artifacts. Efficacy of the algorithm was tested on simulated data with motion containing varying frequency components. We show that even in strongly blurred data, the actual image information remains intact, and the algorithm can identify the phase error and correct it. Furthermore, we use the algorithm to compensate real phase error in FF-SS-OCT imaging of the human retina. Acquisition rates can be reduced by a factor of three (from 60 to 20 kHz frame rate) with an image quality that is even higher compared to uncorrected volumes recorded at the maximum acquisition rate. The presented algorithm for axial motion correction decreases the high requirements on the camera frame rate and thus brings FF-SS-OCT closer to clinical applications.

© 2017 Optical Society of America

**OCIS codes:** (110.4500) Optical coherence tomography; (100.3020) Image reconstruction-restoration.

## References and links

1. P. H. Eichel, D. C. Ghiglia, and C. V. Jakowatz, "Speckle processing method for synthetic-aperture-radar phase correction," *Opt. Lett.* **14**, 1–3 (1989).
2. T. Bonin, G. Franke, M. Hagen-Eggert, P. Koch, and G. Hüttmann, "In vivo Fourier-domain full-field OCT of the human retina with 1.5 million A-lines/s," *Opt. Lett.* **35**, 3432–3434 (2010).
3. D. Hillmann, C. Lührs, T. Bonin, P. Koch, and G. Hüttmann, "Holoscopy–holographic optical coherence tomography," *Opt. Lett.* **36**, 2390–2392 (2011).
4. H. Spahr, D. Hillmann, C. Hain, C. Pfäffle, H. Sudkamp, G. Franke, and G. Hüttmann, "Imaging pulse wave propagation in human retinal vessels using full-field swept-source optical coherence tomography," *Opt. Lett.* **40**, 4771–4774 (2015).
5. D. J. Fechtig, B. Grajciar, T. Schmoll, C. Blatter, R. M. Werkmeister, W. Drexler, and R. A. Leitgeb, "Line-field parallel swept source MHz OCT for structural and functional retinal imaging," *Biomed. Opt. Express* **6**, 716–735 (2015).
6. A. Kumar, T. Kamali, R. Platzer, A. Unterhuber, W. Drexler, and R. A. Leitgeb, "Anisotropic aberration correction using region of interest based digital adaptive optics in Fourier domain OCT," *Biomed. Opt. Express* **6**, 1124–1134 (2015).

7. D. Hillmann, H. Spahr, C. Hain, H. Sudkamp, G. Franke, C. Pfäffle, C. Winter, and G. Hüttmann, "Aberration-free volumetric high-speed imaging of in vivo retina," *Sci. Rep.* **6**, 35209 (2016).
8. D. Hillmann, H. Spahr, C. Pfäffle, H. Sudkamp, G. Franke, and G. Hüttmann, "In vivo optical imaging of physiological responses to photostimulation in human photoreceptors," *Proc. Natl. Acad. Sci. USA* **113**, 13138–13143 (2016).
9. B. Grajciar, M. Pircher, A. F. Fercher, and R. A. Leitgeb, "Parallel Fourier domain optical coherence tomography for in vivo measurement of the human eye," *Opt. Express* **13**, 1131–1137 (2005).
10. Y. Nakamura, S. Makita, M. Yamanari, M. Itoh, T. Yatagai, and Y. Yasuno, "High-speed three-dimensional human retinal imaging by line-field spectral domain optical coherence tomography," *Opt. Express* **15**, 7103–7116 (2007).
11. T. Klein, W. Wieser, L. Reznicek, A. Neubauer, A. Kampik, and R. Huber, "Multi-MHz retinal OCT," *Biomed. Opt. Express* **4**, 1890–1908 (2013).
12. B. Považay, A. Unterhuber, B. Hermann, H. Sattmann, H. Arthaber, and W. Drexler, "Full-field time-encoded frequency-domain optical coherence tomography," *Opt. Express* **14**, 7661–7669 (2006).
13. F. C. Delori, R. H. Webb, and D. H. Sliney, "Maximum permissible exposures for ocular safety (ANSI 2000), with emphasis on ophthalmic devices," *J. Opt. Soc. Am. A* **24**, 1250–1265 (2007).
14. E. N. Leith and J. Upatnieks, "Reconstructed wavefronts and communication theory," *J. Opt. Soc. Am.* **52**, 1123–1128 (1962).
15. U. Schnars and W. P. O. Jüptner, "Digital recording and numerical reconstruction of holograms," *Meas. Sci. Technol.* **13**, R85 (2002).
16. D. Hillmann, G. Franke, L. Hinkel, T. Bonin, P. Koch, and G. Hüttmann, "Off-axis full-field swept-source optical coherence tomography using holographic refocusing," *Proc. SPIE* **8571**, 857104 (2013).
17. T. S. Ralston, D. L. Marks, P. Scott Carney, and S. A. Boppart, "Interferometric synthetic aperture microscopy," *Nature Phys.* **3**, 129–134 (2007).
18. D. L. Marks, T. S. Ralston, S. A. Boppart, and P. S. Carney, "Inverse scattering for frequency-scanned full-field optical coherence tomography," *J. Opt. Soc. Am. A* **24**, 1034–1041 (2007).
19. L. Yu and M. K. Kim, "Wavelength-scanning digital interference holography for tomographic three-dimensional imaging by use of the angular spectrum method," *Opt. Lett.* **30**, 2092–2094 (2005).
20. D. Shabanov, G. Gelikonov, and V. Gelikonov, "Broadband digital holographic technique of optical coherence tomography for 3-dimensional biotissue visualization," *Laser Physics Letters* **6**, 753–758 (2009).
21. S. G. Adie, B. W. Graf, A. Ahmad, P. S. Carney, and S. A. Boppart, "Computational adaptive optics for broadband optical interferometric tomography of biological tissue," *Proc. Natl. Acad. Sci. USA* **109**, 7175–7180 (2012).
22. N. D. Shemonski, F. A. South, Y.-Z. Liu, S. G. Adie, P. Scott Carney, and S. A. Boppart, "Computational high-resolution optical imaging of the living human retina," *Nature Photon.* **9**, 440–443 (2015).
23. K. Kotliar, H. Hanssen, K. Eberhardt, W. Vilser, C. Schmaderer, M. Halle, U. Heemann, and M. Baumann, "Retinal pulse wave velocity in young male normotensive and mildly hypertensive subjects," *Microcirculation* **20**, 405–15 (2013).
24. D. Hillmann, T. Bonin, C. Lührs, G. Franke, M. Hagen-Eggert, P. Koch, and G. Hüttmann, "Common approach for compensation of axial motion artifacts in swept-source OCT and dispersion in Fourier-domain OCT," *Opt. Express* **20**, 6761–6776 (2012).
25. D. Hillmann, *Holoscapy* (Springer Fachmedien Wiesbaden, 2014).
26. M. Wojtkowski, V. J. Srinivasan, T. H. Ko, J. G. Fujimoto, A. Kowalczyk, and J. S. Duker, "Ultrahigh-resolution, high-speed, Fourier domain optical coherence tomography and methods for dispersion compensation," *Opt. Express* **12**, 2404–2422 (2004).
27. P. H. Eichel, D. C. Ghiglia, C. V. Jakowatz, and D. E. Wahl, "Phase gradient autofocus for SAR phase correction: Explanation and demonstration of algorithmic steps," in "Digital Signal Processing workshop, 1992," (1992), pp. 661–662.
28. D. E. Wahl, P. H. Eichel, D. C. Ghiglia, and C. V. Jakowatz, "Phase gradient autofocus - a robust tool for high-resolution SAR phase correction," *IEEE Trans. Aerosp. Electron. Syst.* **30**, 827–835 (1994).
29. C. V. Jakowatz and D. E. Wahl, "Eigenvector method for maximum-likelihood estimation of phase errors in synthetic-aperture-radar imagery," *J. Opt. Soc. Am. A* **10**, 2539–2546 (1993).
30. D. Hillmann, H. Spahr, H. Sudkamp, C. Hain, L. Hinkel, G. Franke, and G. Hüttmann, "Off-axis full-field swept-source OCT and holoscapy," (in preperation) (2017).

## 1. Introduction

The success of Fourier-domain optical coherence tomography (FD-OCT) over time-domain OCT (TD-OCT) was mainly achieved by parallelized detection of depth information. Recently, laterally parallelized FD-OCT techniques have also shown remarkable capabilities going beyond those of scanning FD-OCT systems [2–8]. Imaging multiple lateral points at once reduces the scanning speed or even removes the need for lateral scanning completely. By either using a parallel spectrometer with a 2D camera or a swept laser with a 1D detector, line-field techniques acquire entire sectional images (B-scans) in parallel [5, 9, 10]. Full parallelization is achieved

by a rapidly tunable laser and an area camera, which captures all lateral positions of a volume during a single wavelength sweep. This technique, which we refer to as full-field swept-source (FF-SS) OCT in this paper, thereby provides the highest imaging speeds possible today. The acquisition rate recently reached 39 MHz A-scan rate at 512 pixels in depth, about one order of magnitude faster than most other high-speed OCT approaches [11]. In addition, FF-SS-OCT records volumes that are inherently laterally phase stable, and thereby enables new applications that were previously impossible.

First attempts to fully parallelize FD-OCT with a camera and a tunable laser were reported as early as 2006 by Považay et al. [12]. However, due to limitations of the used laser and the camera technology, the acquired image quality was poor, as compared to that obtained using scanning systems. Nevertheless, it was quickly realized that FF-SS-OCT circumvents limitations imposed by the maximum permissible exposure (MPE) when imaging retina [13] and could therefore increase imaging speed while maintaining the sensitivity. Consequently, by using a high-speed camera in a full-field setup, Bonin et al. first demonstrated retinal images [2].

Still, image quality in all parallelized approaches is lower compared to scanning OCT. First introduced in holography by Leith and Upatnieks [14] and later adapted for digital holography, [15] off-axis techniques can improve image quality when applied to parallelized OCT [5, 16]. In particular, coherence noise and artifacts were reduced in the images, when applying the respective off-axis filters. As an additional advantage, the off-axis reference enables full-range imaging and thus doubles the effective measurement depth. On the downside, lateral oversampling is required and not every camera pixel carries independent information about the sample, i.e., the number of independent pixels in the OCT is lower than the amount of pixels of the camera.

Early on FF-SS-OCT development, the resulting fast and phase-stable acquisition that is inherent to full-field techniques also suggested the use of holographic reconstruction techniques. These rely on the signal phase, which is not corrupted in FF-SS-OCT by the sample motion between A-scans. However, despite difficulties in obtaining phase stable data, algorithms for correcting defocus and increasing the depth of focus were first demonstrated with scanning OCT on static samples, in a technique that became known as interferometric synthetic aperture microscopy (ISAM) [17]. Holographic reconstruction on full-field swept-source data was at first only demonstrated mathematically, probably due to missing experimental systems [18]. Later, holoscopy and similar techniques showed a fully parallel acquisition combined with suitable reconstruction techniques, allowing for depth independent sensitivity and resolution [3, 19, 20].

Since defocus is only a special image aberration, higher aberration orders were also corrected, first for scanned [21, 22] and later for full-field data [6, 7]. Numerical correction of aberrations in full volumes of the human retina was finally demonstrated in vivo by FF-SS-OCT [7]. To this end, volume rates of more than 100 Hz were required to overcome the rapid movements of the living human eye. Nerve fibers, capillaries, and single photoreceptor cells were imaged with diffraction-limited resolution at a 7 mm pupil diameter. Contrary to traditional adaptive optics using deformable mirrors and wavefront sensors, correction was performed numerically after the data had been acquired. In addition to previously demonstrated numerical aberration correction on scanned en-face OCT images of the human retina [22], the full-field technique provides entire volumes of living human retina, from which multiple layers with diffraction limited resolution can be extracted.

FF-SS-OCT gives complete access to the phase of light scattered from a volume of tissue. Besides aberration and defocus correction, numerical manipulation of the detection aperture and interferometric measurements of small changes in geometry or the refractive index of the sample are possible. This was recently demonstrated in two publications. First, by evaluating phase data, off-axis full-field swept-source OCT (OA-FF-SS-OCT) was used for imaging heartbeat-induced pressure waves within the retina and even measure their velocity [4]. Previous measurements in this area used classical retinal fundus imaging, where a subsequent segmentation of blood vessel

walls showed their pulsation [23]. The pulse wave velocities measured with OA-FF-SS-OCT deviated from these earlier measurements by several orders of magnitude, but were in accordance with those values expected from theory and observed in other vessels of the human body. This detection of pressure waves in the human retina could have important applications, since it allows a non-invasive determination of biomechanical properties of the vascular system.

Second, full-field swept-source OCT (FF-SS-OCT) was applied to measure intrinsic optical signals in living human retina; this was a tremendous improvement over previous measurements with scanning systems [8]. For the first time, a significant change of the optical path length of the outer segment was shown by analyzing the phase of the scattered light. With only a few microwatts per square millimeter white-light stimulation, the optical path through the light-sensitive part of the photoreceptor cells changed by several 100 nm in a few hundred milliseconds. As with the pulse-wave detection, these intrinsic optical signals can prove valuable in early diagnosis of many retinal diseases.

These new applications are based on the absolute lateral phase stability of each frame (or wavelength). However, even with high-speed cameras, FF-SS-OCT is vulnerable to motion induced axial phase errors, since only the lateral information is encoded in the individual images, and depth information is measured time-encodedly during the wavelength sweep of the tunable light source. Therefore, axial motion causes a loss of signal and a reduction of axial resolution, which can be corrected when known. In this paper we introduce an algorithm that uses the simultaneous acquisition of the phases at all lateral positions to estimate the motion-associated phase error for a correction of the imaging artifacts. The motion correction algorithm was tested with simulated data and real images of the human retina. Increase of resolution and image quality is demonstrated. The approach thereby overcomes the limitation of FF-SS-OCT to require extremely high frame rates needed for in vivo retina imaging.

## 2. Axial phase errors in parallelized FD-OCT

Motion that occurs during the acquisition of the volume causes characteristic artifacts in the reconstructed volume, which are equivalent to group velocity dispersion (GVD) mismatch between reference and sample arm [24]. For example, acquisition of a single depth profile with an axial motion described by constant velocity  $v$  that moves over a depth  $\Delta z$  during the entire sweep results in the following modified cross-correlation term as a function of the time  $t$ :

$$I(t) \propto \cos[2k(t)z(t)] = \cos\left[2\left(m_k\left(z_0 + \frac{k_i}{\Delta k}\Delta z\right)t + m_k vt^2 + k_i z_0\right)\right], \quad (1)$$

where  $k(t)$  is the wavenumber sweep,  $z(t) = z_0 + vt$  is the axial motion,  $T$  is the total sweep and measurement time,  $\Delta k$  is the wavenumber sweep range,  $m_k = \Delta k/T$  is the sweep rate, and  $k_i$  is the initial wave number. This equation demonstrates that linear motion causes a shift of the image that is amplified by a factor  $k_i/\Delta k$ , while the image quality, i.e., the axial resolution, is only slightly degraded by the term  $m_k vt^2$ . However, if the actual motion is non-linear, the blur in the  $z$ -direction is also amplified by the factor  $k_i/\Delta k$ , leading to significant motion artifacts. So far, to avoid those artifacts, high acquisition rates of 60 kHz frame rate (for 512 recorded wavelengths) were necessary to obtain useful retina images and even at these frame rates, small artifacts remain. These required high acquisition rates are probably the most hindering part when it comes to adopting this technology for wide spread applications.

Since dispersion mismatch of the reference and sample arm causes phase errors similar to those induced by motion, different well-known algorithms can be used to compensate them. Both, dispersion and axial motion blur effects can be reverted by multiplying a correcting spectral, i.e.,  $k$ -dependent phase to the complex interference spectrum. For dispersion artifacts, the correcting phase function is often calculated from calibration measurements. However, since those calibration measurements have to be implemented on a specific fixed sample, e.g., a

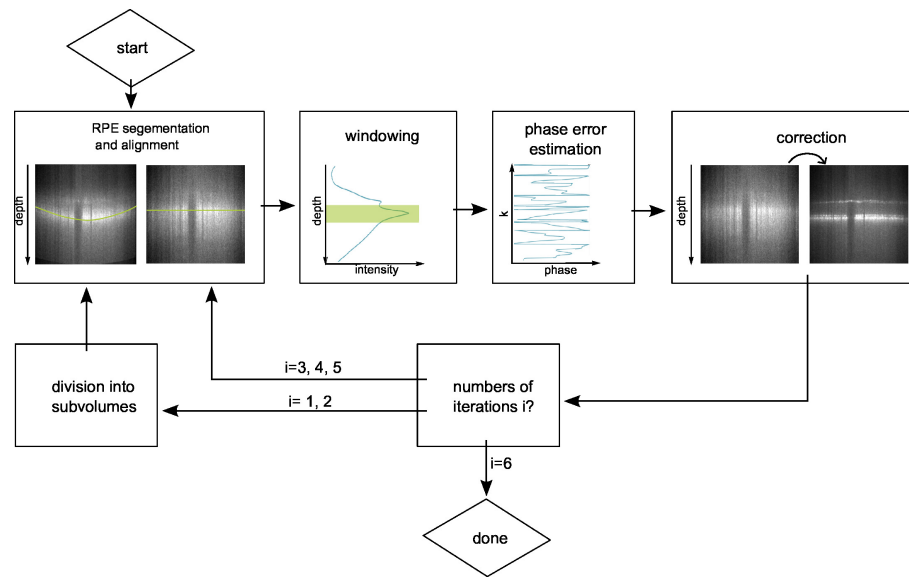


Fig. 1. Schematic of the algorithm used for motion correction. The first two iterations ( $i = 1, 2$ ) are used for compensating global motion. Further iterations ( $i = 3, 4, 5$ ) are used to compensate rotational motions. After the fifth iteration the algorithm was finished.

mirror, they only detect the phase error caused by the setup and are therefore not suited for compensating artifacts caused by sample motion. To overcome this problem other algorithms were developed [24–26], e.g., based on short-time Fourier transforms or the optimization of image quality. Improvements in image quality vary. Common to all previously published approaches is their limitation to low-order phase errors, which can be represented by a limited set of coefficients. Usually, this is sufficient for dispersion mismatch and moderate motion, but rapidly changing motion has so far not been successfully corrected.

### 2.1. The phase gradient autofocus algorithm

First established for synthetic aperture radar (SAR), the phase gradient autofocus (PGA) algorithm [1, 27, 28] estimates an arbitrary correcting phase error that is not restricted to a few degrees of freedom, and therefore can correct even high-frequency motion. In the PGA algorithm, the estimation of the present phase error is completely based on the phase information contained in the data and an appropriate statistical model describing the behavior of the signal and the noise. Thus, it is possible to correct even data with poor image quality while increasing the signal-to-noise ratio (SNR) in the process. In the present study, we adopted the algorithm to correct motion for FF-SS-OCT and test its efficacy and motion frequency dependency by simulating motion in OCT data of the human retina. Furthermore, we demonstrate with real full-field swept-source data that using this modified PGA algorithm can reduce the required acquisition rate by a factor of three from 60 to 20 kHz frame rate, without sacrificing image quality. At this reduced acquisition rate the entire field of view of the implemented high-speed camera (FASTCAM SA-Z, Photron) can be read out, or a transition to less expensive cameras becomes possible.

The PGA algorithm is based on the hypothesis that the phase error is redundant, i.e., equal in all A-scans of the entire volume or at least in a sufficiently large part of it. This assumes that all lateral structures move with the same axial velocity, which is reasonable considering their simultaneous acquisition. Under this condition a single spectrum  $\mathbf{x}_l = \{x_{l,n}\}$  at the lateral



position  $l$  could be described by

$$x_{l,n} = A_{l,n} e^{i\Phi_{l,n}} e^{i\Phi_{\text{error},n}} + u_{l,n}, \quad (2)$$

where  $n$  is the axial pixel position,  $A_{l,n}$  describes the amplitude and  $\Phi_{l,n}$  is the phase of a dominant point scatterer, which both depend on  $l$ . The axial phase error  $\Phi_{\text{error},n}$  is common to all A-scans and therefore independent of  $l$ . The last term  $u_l = \{u_{l,n}\}$  describes uncorrelated signal contributions and noise. The phase error is connected to the point spread function (PSF) via a Fourier transform. Hence, we used a statistical model to estimate the common axial PSF of all A-scans, while reducing the impact of noise and overlapping PSFs of adjacent structures. For this, the model assumes that these two effects are uncorrelated for all lateral positions. Finally by applying a Fourier transformation to the PSF, the phase error is obtained and motion artifacts are then compensated by multiplying the complex interference spectrum of the image data with the complex conjugate of the estimated phase error.

The procedure for estimating the phase error is divided into several iteratively applied steps as shown in Fig. 1. In the first two iterations the motion induced phase error that is common for the whole field of view is calculated and corrected. However, retina measurements are also corrupted by locally varying motions, caused by eye rotations. The rotation causes slowly and smoothly varying axial motion vectors at different lateral position of the field of view. However, the change in this motion vector is smooth and thus the motion vector can be assumed to be constant within a certain region and should only change over greater distances. Therefore, in the three additional iterations the volume was divided into smaller sub-volumes and the phase error was calculated for each sub-volume separately. During each iteration the size of the sub-volumes is reduced to correct the local motion more precisely. However, the size of the sub-volumes was limited by noise and PSF overlap, which became dominant when the number of evaluated A-scans became too small.

The estimation of the phase error in each iteration starts with a determination of the dominant point scatterer for each lateral position (A-scan). For this purpose, the brightest layer in the image, carrying the largest amount of energy is selected, since its phase dominates other phase contributions. To avoid errors caused by speckle-induced intensity variation, a continuous and smooth layer carrying the highest amount of signal energy is segmented. In retinal imaging, this is in general the retinal pigment epithelium (RPE), which is consequently segmented as a first step. Since this layer is curved, and the signals from which the phase error is derived are in different depths, the corresponding interference spectra show different modulation frequencies in the Fourier domain. To remove this depth-dependent modulation frequency for the following computations, we circularly shift each A-scan with the Fourier shift theorem accordingly and place the RPE at the zero-delay-line of the volume. However, due to the layered structure of the retina, OCT signals from other layers may be partially correlated, and these layers can bias the estimation of the phase error in the PGA algorithm. To avoid the influence of layers adjacent to the RPE, the newly arranged volume is next windowed in the axial dimension around the central peak.

Thereby, a major challenge is the selection of the optimal window size, which is always a trade-off between removing data that do not contribute to the phase error estimation and isolating the point spread function. With regard to that, the window size is determined from an average A-scan of the volume as the width of the presently blurred signal of the RPE. Since the blur in each iteration decreases after correcting the phase error, the window size should be adapted in all iterations, before determining the phase error again. Thus, in each iteration, the accuracy of the determined phase error increases, since the influence of signals adjacent to the RPE decreases.

There are multiple approaches for actually calculating the phase error functions from the

windowed A-scans. The most intuitive one is a simple averaging of all spectra according to:

$$\Phi_{\text{error},n} = \arg \sum_{l=1}^N x_{l,n} \quad (3)$$

$$= \arg \sum_{l=1}^N \left( A_{l,n} e^{i\Phi_{l,n}} e^{i\Phi_{\text{error},n}} + u_{l,n} \right), \quad (4)$$

where  $N$  is the number of lateral positions. Due to the axial shifting of the dominant scatterer (RPE) to the zero-delay the phase of the term  $A_{l,n} e^{i\Phi_{l,n}}$  becomes zero for all lateral positions  $l$ . The other signals and noise,  $u_{l,n}$ , sum up to zero if they are uncorrelated. By this means the phase error common in all A-scans, like the one caused by axial motion add up coherently, while all uncorrelated phases cancel each other out. Unfortunately in most cases the phases of  $u_{l,n}$  are not completely uncorrelated, even after the axial spectral windowing. Therefore the phase of a simple averaged spectra would still contain contributions of the term  $u_{l,n}$ .

The most effective way to calculate the phase error is to our knowledge, to use the maximum likelihood estimation (MLE). This approach also uses the statistic of the A-scans combined with an appropriate statistical model for the signal and noise to eliminate the unwanted phase from the resulting phase error function. Compared to Eq. (4) this approach leads to a quicker convergence of the algorithm. It was shown, that for this model, the phase error with maximum likelihood is approximately given by the eigenvector of the highest eigenvalue of the spectrum covariance matrix in the frequency domain [29]. Thereby, the estimation of the covariance matrix  $\hat{C}$  is calculated by

$$\hat{C} = \frac{1}{N} \sum_{l=1}^N x_l x_l^H, \quad (5)$$

where  $H$  indicates the hermitian transpose matrix. Finally, phase of the respective eigenvector, i.e., the most likely phase error, is then used to compensate the motion blur. A more detailed description and the derivation of this result are found in [29].

### 3. Materials and methods

To test the algorithm, data are acquired using a full-field swept-source OCT system as shown in Fig. 2. The setup, which is described in detail elsewhere [4, 30], is based on a Mach-Zehnder interferometer. The illumination of the tunable light source (Superlum Broadsweeper BS 840, 50 nm sweep range, 841 nm central wavelength) is split into reference and sample wave, where the sample illumination contains 5 mW radiant power. For a collimated illumination of the retina a focus was generated in the outer focal plane of the eye using an achromatic lens. The light backscattered from the retina is imaged onto the camera and recombined with the reference wave, which is incident at an angle of  $1.2^\circ$  with respect to the optical axis (off-axis geometry [30]). At an acquisition rate of 60 kHz only the central  $896 \times 368$  pixels can be read out. During each sweep 512 images are taken, leading to a maximum volume rate of 117 Hz at a 60 kHz frame rate. For lower acquisition rates, the volume rate is accordingly reduced, too, but the same field of view is used.

To investigate the precision of the implemented algorithm in detecting motion-induced phase errors, a 3D image of a retina containing no motion artifacts is artificially blurred. The data are taken from a young male volunteer at the highest possible frame rate of 60 kHz. At this acquisition rate, the volume contains nearly no motion artifacts. To remove the remaining phase error, the volume is corrected using the PGA algorithm until no phase error can be detected. Figure 2(b) shows a B-scan of the corrected original volume. To introduce a blur numerically, an arbitrary but known phase error is created, with random but equally distributed phases between  $-\pi$  and  $+\pi$

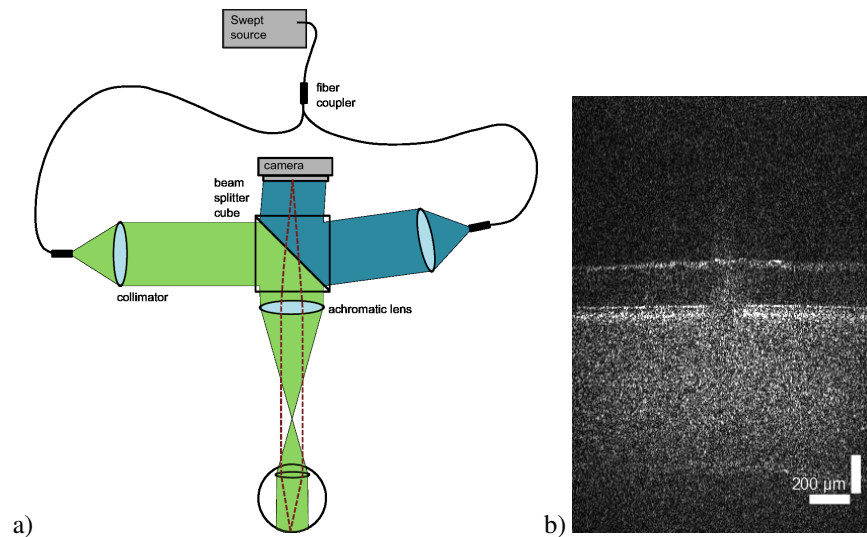


Fig. 2. a) The setup for FF-SS-OCT imaging of the retina. The tunable laser light is split into sample illumination (green) and reference illumination (blue). The backscattered light (dashed red line) of the sample is superimposed with the reference illumination on the camera sensor. b) B-Scan from a single volume with no remaining artifacts due to global motion. The volume is recorded in 8 ms corresponding to a frame rate of 60 kHz, and afterwards corrected using the modified PGA algorithm until no further phase error can be detected. This image serves as reference when simulating motion artifacts.

for all spectral frames. To investigate the frequency dependency of the algorithm effectiveness, high frequencies in the phase error function are gradually removed using a Gaussian filter. The widths of the Gaussian filters are chosen, such that the phase broadens the axial point spread function by a full width at half maximum (FWHM) ranging from 2078 px to 0.5 px, where the total axial volume size is 433 px. The phase error function resulting in a PSF with a FWHM of 2078 px contains all possible frequencies up to the Nyquist frequency and should therefore simulate the worst-case scenario, whereas, at 0.5 px FWHM, only a linear phase shift remains, which only leads to an axial shift of the image, but no degradation of the image quality.

To investigate the performance of the PGA algorithm with real motion artifacts, retina images of the same young male volunteer are examined for 15 different acquisition rates ranging from 1 to 60 kHz camera frame rate. The measured volumes are corrected in five iterations. Thereby, the first two iterations are used to compensate the global phase error in the entire volume; the following three iterations also compensate the rotation by dividing the volume into two, eight, and 32 sub-volumes, respectively. The corresponding minimal sub-volume size is  $38 \times 30$  pixels ( $228 \mu\text{m} \times 180 \mu\text{m}$ ).

#### 4. Results

Introducing a random phase noise to the spectral dependence of the interference pattern eliminates the information in the intensity image completely (Fig. 3(a)). No retinal structures are visible with a PSF width of 2078 px, which is more than four times wider than the size of the image. Astonishingly, even though the phase error is completely random, the modified PGA algorithm is able to reconstruct a faint structure of the RPE. In an image degraded by a low-pass filtered phase noise to a PSF width of 130 px, the IS/OS junction and RPE, as well as the surface of the nerve fiber layer, become visible after motion correction, although the uncorrected images show only speckle noise (Fig. 3(b)). With an image degradation leading to a 16 px-wide PSF, the PGA



algorithm can completely restore the structures visible in the ground truth images (Fig. 3(c)).

To quantify the error made by the PGA algorithm, the difference between the estimated and the actual phase error is calculated. For this, the phase error estimations of all five iterations are summed up to give the total phase error before the phase difference is actually computed. The phase difference functions are then unwrapped, and the linear part is removed, since it only affects the position of the images. After this, the phase differences are weighted using a Hann window, since the spectra have also been multiplied with a Hann window during image reconstruction. To quantify the error made by the PGA algorithm, the absolute values of the phase differences are averaged over the complete wavelength range. The resulting errors are shown in Fig. 4(a) for the different widths of the PSF. Up to a PSF width of 10 px, a complete correction of the simulated motion blur is possible. Beyond this, the residual phase error increases and the PGA algorithm cannot restore the complete image information. For a further quantification of the resulting image quality, the SNR of the artificially blurred volumes and that of the corrected volumes are calculated (Fig. 4(b)). For this purpose, all A-scans of a volume are axially aligned and averaged. For the SNR estimation, the ratio of the maximum signal at the RPE and the average signal in the upper 100 data points, a region above the retina that contains only noise, is calculated. A negligible systematic bias is incorporated into the calculation that prevents the calculated SNR to fall to 0 dB. Without motion correction, the SNR drops continuously as the motion blur broadens the PSF. Above a width of 100 px, the SNR is close to 0 dB. Motion correction is able to maintain the SNR up to a PSF width of 10 px and even at maximum blur, a SNR of 3 dB is obtained.

The results of the compensated real motion in retinal imaging are shown in Fig. 5 for volumes taken at frame rates of 60 kHz, 20 kHz, and 3 kHz, respectively. To improve the image quality, 50 volumes obtained in one shot are averaged incoherently using their magnitude without phases. At all frame rates, improvement of the image quality is possible, given optimal image quality at 60 kHz and 20 kHz frame rates. At 3 kHz, a significant improvement of the image quality is possible, but considerable motion blur remains after correction. This is also visible in the SNR of the images with and without motion correction (Fig. 6), which is calculated in the same way as the SNR of the simulations is.

## 5. Discussion

Contrary to scanning OCT, in FF-SS-OCT the slowest process is not the lateral sampling, but the spectral sampling. Consequently, axial motion has the largest effect on the obtained images and results in a decrease in axial resolution and SNR. Strong motion can even make the obtained images completely useless. Luckily, due to the coherent nature of the imaging process, loss-less correction of motion blur is in principle possible, if the motion is known and the interference signal is sampled correctly. However, in real imaging situations there is no direct information on the tissue motion and the correcting phase function has to be retrieved from the recorded data. Here, we demonstrate that the modified PGA algorithm allows in many scenarios estimating the required phase errors.

In the simulated data, all information describing the retinal structure is still contained in the volumes and is in principle accessible. Although the volumes disturbed by a PSF of 2078 px and 130 px FWHM seem to contain only noise and therefore no structure to start the estimation with, the corresponding averaged A-scans of these volumes show that there is a slight signal maximum, which appears to provide enough information for the algorithm to compensate the phase error resulting in the presented data. Therefore, our algorithm is capable of estimating the phase error, even for extremely poor image quality and without increased computation time for strong motion. . With simulated data, PGA reaches an improved SNR by up to 5 dB, even for strongly blurred volumes. The main structures (nerve fiber layer, inner-segment outer-segment membrane, and RPE) can still be reconstructed for a PSF of 130 px FWHM, whereas in the completely blurred volume (PSF of 2078 px FWHM), it is only possible to reconstruct a coarse

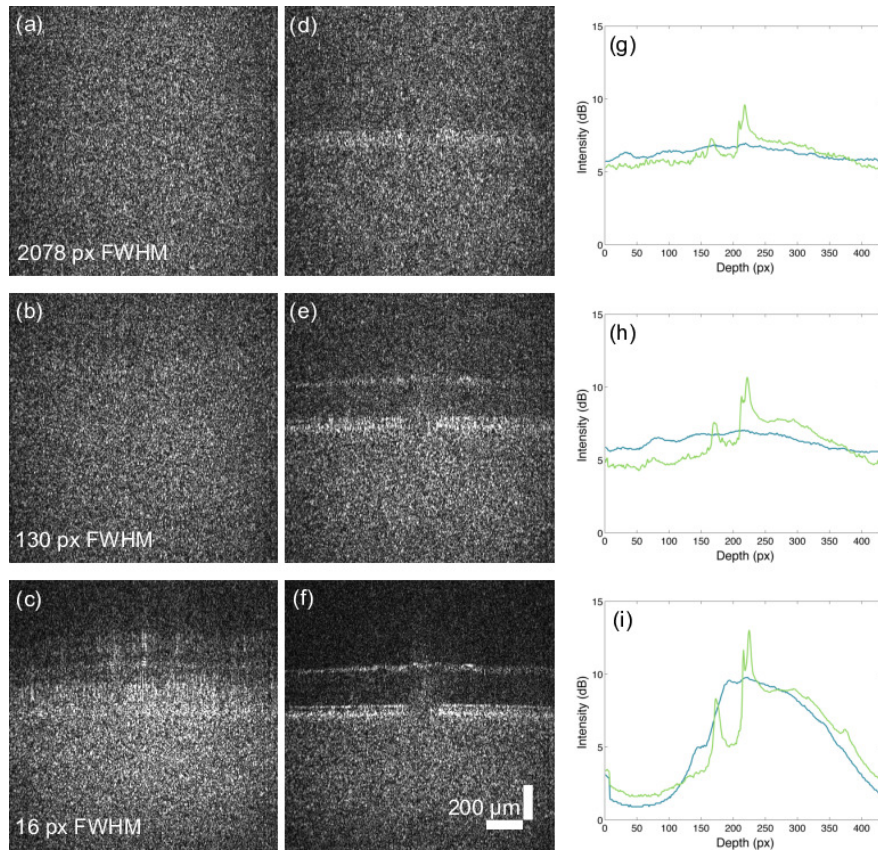


Fig. 3. B-Scans of the investigated volume with the simulated motion (a-c) and after the correction (d-f). (g-i) Corresponding laterally averaged datasets before and after correction. The simulated motion corresponding to a PSF with FWHM of (a, d, g) 2078 px, (b, e, h) 130 px, and (c, f, i) 16 px.

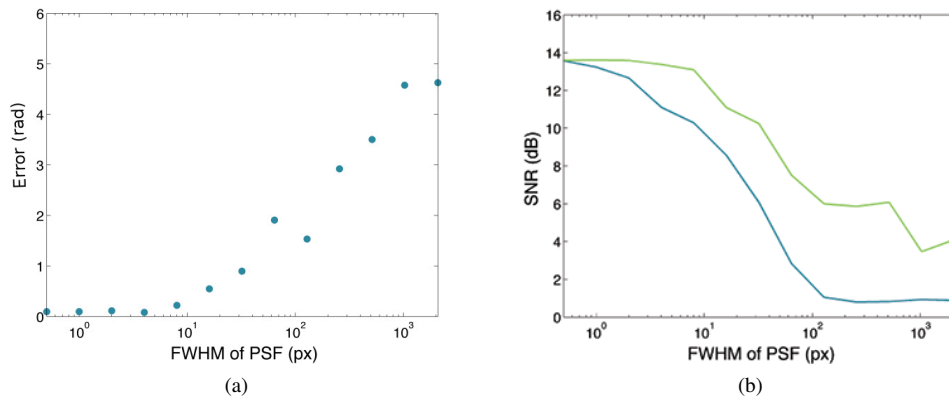


Fig. 4. (a) The remaining averaged phase error after correction with the PGA algorithm for different strong motion blur, broadening the axial PSF from initially 0.5 px to 2078 px FWHM; axial size of the image is 433 px. (b) Resulting SNR for the uncorrected (blue) and corrected images (green)

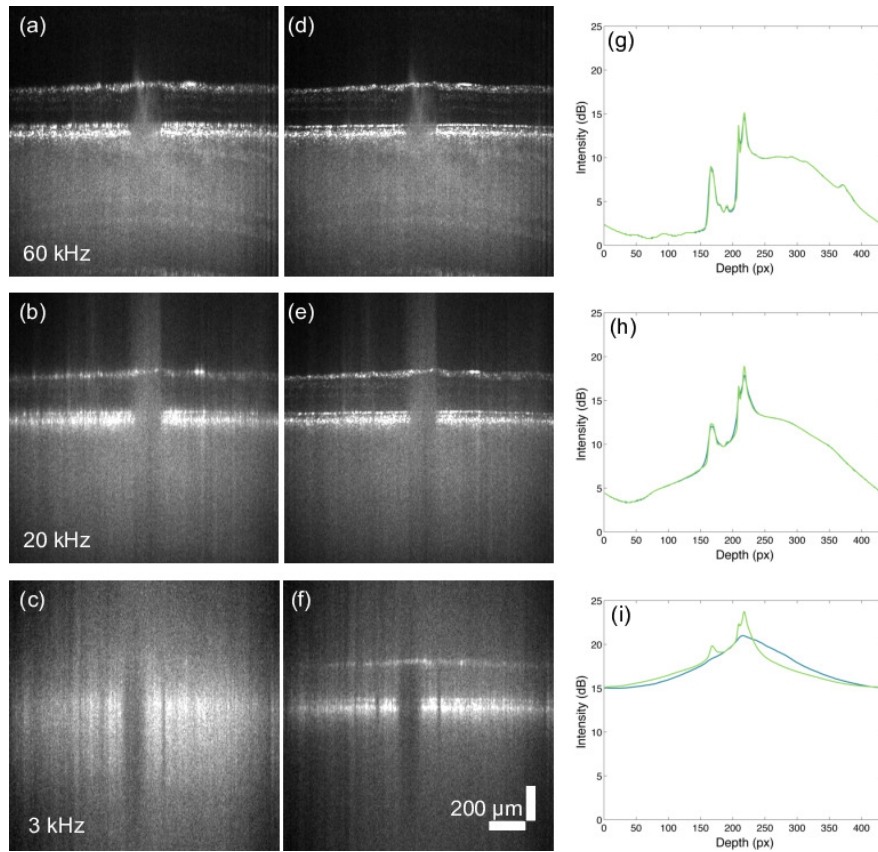


Fig. 5. B-Scans from volumes of human retina without motion correction (a-c) and after motion correction (d-f). (g-i) Corresponding laterally averaged datasets before and after correction. OCT volumes are recorded at 60 kHz frame rate (a,d, g), 20 kHz frame rate (b, e, h), and 3 kHz frame rate (c, f, i) and averaged 50 times to improve the image quality.

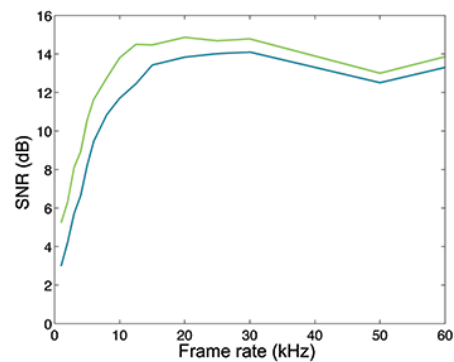


Fig. 6. SNR at different frame rates for the uncorrected volumes (blue) and motion corrected volumes (green).

structure representing the RPE.

When correcting real retinal volumes, an increase of the image quality and the SNR about 1 dB to 3 dB is achieved for all acquisition rates. Even at a 60 kHz frame rate (corresponding to 117 volumes per second), the image quality increases. Previously, we used this imaging speed to reduce motion effects, since we assumed that motion artifacts were negligible in that case. Surprisingly, best SNR was achieved at a frame rate of 20 kHz (39 volumes per second), because the SNR of the OCT signal increased due to the longer integration time of the camera. For this imaging rate, the algorithm enhanced the depth resolution and an additional layer appeared, representing the boundary layer of the photoreceptors between the inner-segment/outer-segment membrane (IOS) layer of the photoreceptors and the RPE. Hence, motion correction cannot only decrease the camera frame rate, but it can even improve the image quality. Additionally, the image quality could be improved by compensating rotations using several sub-volumes that were corrected independently. While this approach corrects coarse local motion, artifacts such as those created by blood flow remain. Blood flow is not a constant motion over the entire depth and the volumes which are affected by the same phase error are too small for calculating a correcting phase. Hence it seems very unlikely that motion blur in the vessels can be corrected this way. However, for our purpose the approach to correct local motion was effective in increasing the image quality in addition to the improvements by the global phase error compensation.

Nevertheless, for lower acquisition rates, both image quality and measured SNR decrease rapidly, although the main structures of the retina remain visible. In vivo, the algorithm is less effective compared to simulated data with equivalent blur. This has multiple reasons: first, this is caused by lateral motion, which becomes more severe with low frame rates and is not considered by our algorithm. Second, the lack of compensation for differential motion, e.g., caused by the pulsation of the blood vessels in the retina. And finally, additional effects of fast and strong motion during the acquisition, such as fringe washout and undersampling that additionally degrade the data by an increase in noise and a loss in signal. Thus, information in the acquired data is destroyed and therefore, the algorithm is only capable to reconstruct the image approximately. Hence, a further reduction of the acquisition time is not possible even with a perfect numerical correction.

However, an error remains in the simulations and for correctly sampled in vivo measurements. The windowing step, which is necessary to minimize the influence of adjacent signals, ultimately causes high frequencies not to be taken into account when estimating the phase error. Consequently, the layered structure of the retina is an extremely difficult target using PGA, since significant signals of the other layers remain in the direct neighborhood and cannot be suppressed by windowing of a single peak. But despite these difficulties, PGA is capable to estimate the phase error and improve image quality significantly. Furthermore, due to the layered structure of the retina, too, different A-scans of the retina are somewhat correlated, and the statistical model used for the phase estimation does only hold approximately.

## 6. Conclusion

Numerical motion correction reduces the acquisition rate in FF-SS-OCT of human retina by a factor of three from 117 to 39 volumes per second (60 kHz to 20 kHz frame rate), without sacrificing image quality. At this acquisition rate the entire camera sensor ( $1024 \times 1024$  pixels) of our camera can be read out and, therefore, the lateral space-bandwidth product can be increased. Hence, either the field-of-view can be enlarged or the resolution can be improved. Thus using motion correction gives more flexibility to the design of FF-SS-OCT setups and the choice of the high-speed camera. In addition, by increasing the exposure, the image quality can also be improved, getting closer to those of scanned systems.

Finally, given the strongly blurred data of the simulations or those of slowly acquired volumes, it is remarkable how much information the PGA autofocus can reconstruct, and, as consequence,

how much information is left in the blurred FF-SS-OCT volumes. Even without any visible axial structures, the algorithm is able to distinguish at least the nerve fiber layer from the RPE.

### **Funding**

This research was sponsored by the German Federal Ministry of Education and Research (Innovative Imaging & Intervention in early AMD, contract numbers 98729873C and 98729873E).